

See discussions, stats, and author profiles for this publication at: <https://www.researchgate.net/publication/51470621>

Correlated Optical Measurements and Plasmon Mapping of Silver Nanorods

ARTICLE *in* NANO LETTERS · AUGUST 2011

Impact Factor: 13.59 · DOI: 10.1021/nl202027h · Source: PubMed

CITATIONS

64

READS

36

10 AUTHORS, INCLUDING:



Beth Guiton

University of Kentucky

25 PUBLICATIONS 833 CITATIONS

SEE PROFILE



Vighter Iberi

Oak Ridge National Laboratory

9 PUBLICATIONS 156 CITATIONS

SEE PROFILE



Paul G Kotula

Sandia National Laboratories

236 PUBLICATIONS 2,806 CITATIONS

SEE PROFILE



Maria Varela

382 PUBLICATIONS 5,252 CITATIONS

SEE PROFILE

Correlated Optical Measurements and Plasmon Mapping of Silver Nanorods

Beth S. Guiton,^{*,†,‡} Vighter Iberi,[§] Shuzhou Li,^{||} Donovan N. Leonard,^{†,⊥} Chad M. Parish,[†] Paul G. Kotula,[#] Maria Varela,[†] George C. Schatz,[∇] Stephen J. Pennycook,^{†,○} and Jon P. Camden^{*,§}

[†]Materials Science and Technology Division, Oak Ridge National Laboratory, Oak Ridge, Tennessee 37831, United States

[‡]Department of Chemistry, University of Kentucky, Lexington, Kentucky 40506, United States

[§]Department of Chemistry, University of Tennessee, Knoxville, Tennessee 37996, United States

^{||}Division of Materials Science, School of Materials Science and Engineering, Nanyang Technological University, Singapore, 639798

[⊥]Department of Materials Science and Engineering, University of Tennessee, Knoxville, Tennessee 37996, United States

[#]Materials Characterization Department, Sandia National Laboratories, Albuquerque, New Mexico 87185, United States

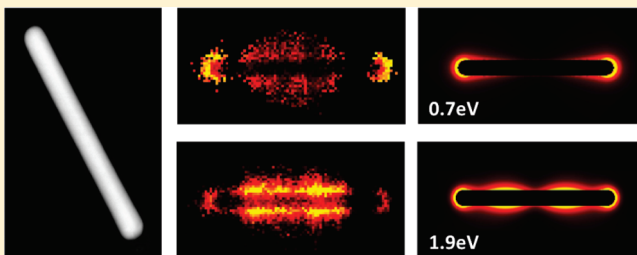
[∇]Department of Chemistry, Northwestern University, Evanston, Illinois 60208, United States

[○]Department of Physics and Astronomy, Vanderbilt University, Nashville, Tennessee 37235, United States

 Supporting Information

ABSTRACT: Plasmonics is a rapidly growing field, yet imaging of the plasmonic modes in complex nanoscale architectures is extremely challenging. Here we obtain spatial maps of the localized surface plasmon modes of high-aspect-ratio silver nanorods using electron energy loss spectroscopy (EELS) and correlate to optical data and classical electrodynamics calculations from the exact same particles. EELS mapping is thus demonstrated to be an invaluable technique for elucidating complex and overlapping plasmon modes.

KEYWORDS: Plasmonics, EELS, STEM, discrete dipole approximation, Rayleigh scattering, multivariate statistical analysis



The collective oscillation of the conduction electrons in a metallic nanostructure, commonly excited by coupling to an electromagnetic field, is known as a localized surface plasmon (LSP).¹ These oscillations have frequencies and intensities which are highly sensitive to the shape, size, and dielectric environment of the nanostructure,² leading to a plethora of related applications such as photonic circuits,³ wave-guiding on subdiffraction limit length scales,⁴ and chemical and biological sensing;⁵ plasmon excitation also leads to local enhancements of incident electromagnetic fields of several orders of magnitude, enabling the spectroscopic detection of single molecules.^{6–8} Utilizing such materials requires intimate understanding of the relationship between the structure and the optical response of the material, which requires a characterization technique capable of elucidating the structure and functionality of the particle on the nanometer and subnanometer length scale. With the recent proliferation of aberration-corrected and monochromated transmission electron microscopes (TEMs), electron microscopy techniques—specifically electron energy loss spectroscopy (EELS) in the scanning transmission electron microscope (STEM), and energy filtered TEM (EFTEM)—have re-emerged as unique tools to map the energy and spatial distribution of metallic nanoparticle plasmon modes on length scales relevant to the application of the LSP oscillation.^{9–22}

While it is clear that LSPRs can be excited by both far-field optical excitation and fast moving electrons, the detailed connection between resonance-Rayleigh scattering, EELS mapping, and electrodynamics remains unexplored at the single particle level. Studies correlating these measurements are especially important, therefore, if the fundamental connection between EELS derived data and optically driven plasmons is to be elucidated. Theoretical studies have shown that the photonic density of states is related to the EELS intensity,²⁰ although it has been cautioned that a quantitative description of this coupling may not be possible.²³ The complexity of the experiment is increased further for high-aspect-ratio nanostructures, where data interpretation becomes challenging due to the many LSP components—both longitudinal and transverse.²⁴ Moreover, the “dark” modes of these particles are of fundamental interest for applications such as subdiffraction limit wave-guiding without radiative loss; a method to extract the rich and complex data from these systems is therefore urgently needed.

Here we present EELS mapping of plasmon modes for a series of silver nanorods, correlated for the first time to optical data taken from the exact same particles, and electrodynamics

Received: June 16, 2011

Revised: July 1, 2011

Published: July 06, 2011

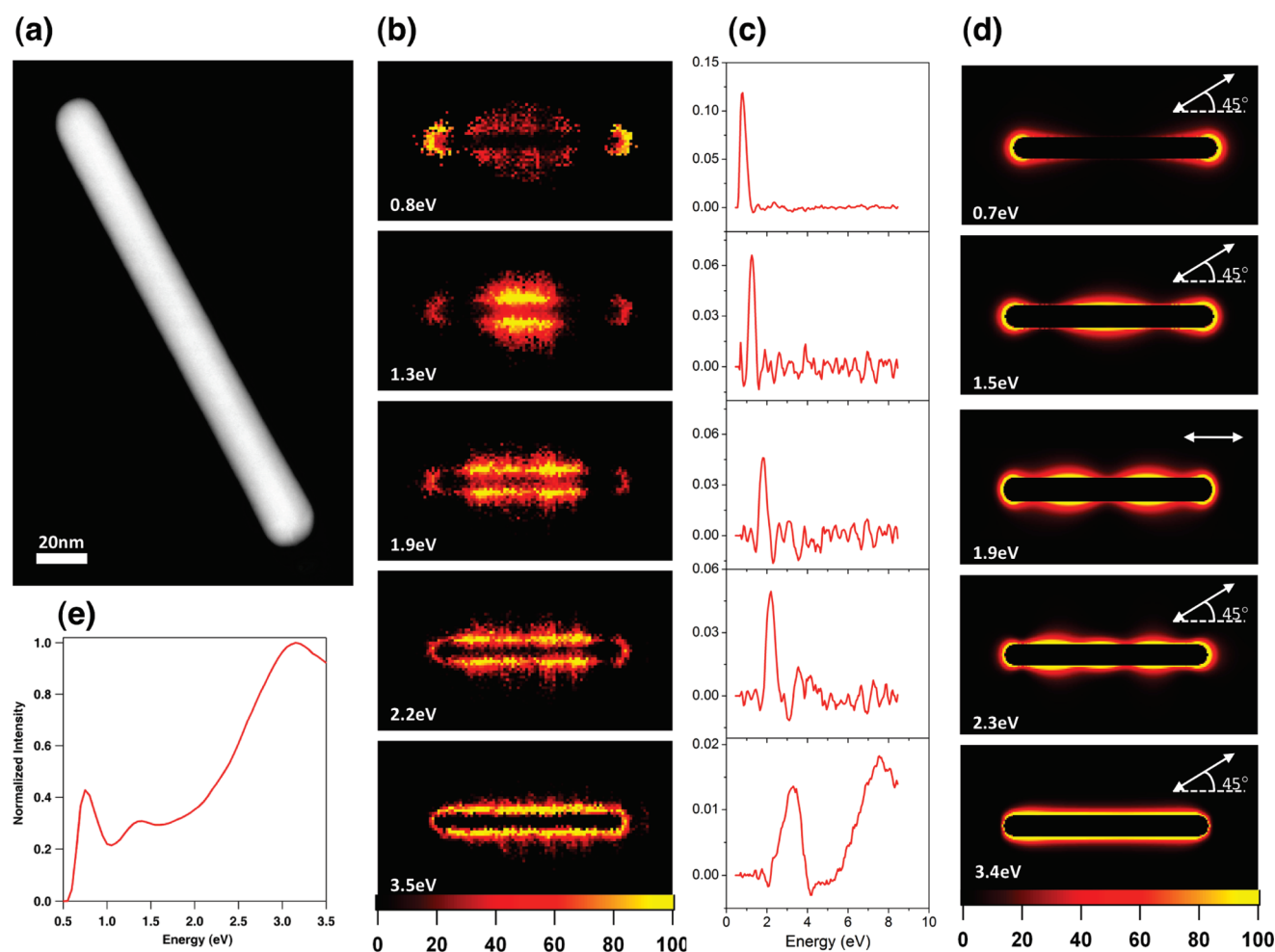


Figure 1. EELS data and electrodynamic calculations for rod 1. (a) ADF image of the rod: length = 192 nm, diameter = 20 nm, aspect ratio = 9.6. (b) MVSA score images, and (c) loading spectra, for each component, interpreted as plasmon maps and energies, respectively. From a total of 12 components found by MVSA, four components were considered overlapping and combined to form the $E = 0.8$ eV mode, two were combined to form the $E = 3.5$ eV mode, and three are displayed as found. (d) DDA calculated electric field plots displaying the field generated by a plane wave optical excitation at the energies and polarizations given on each panel. (e) Summed EEL spectrum.

simulations utilizing the experimental geometries. Remarkably, we find that the many plasmon modes characteristic of high-aspect-ratio particles can be reliably extracted using multivariate statistical analysis (MVSA). Further, the modes so identified are in excellent agreement with local field maps obtained using plane-wave excitation and classical electrodynamic modeling. Moreover, the main features of the resonance Rayleigh scattering spectra from the correlated nanostructures are captured by the electrodynamic simulations, reinforcing the powerful connection between electron and optical excitation of plasmon modes. Similar components are resolved using both conducting (C) and insulating (SiN_x) substrates.

Samples were prepared by depositing commercially available solutions of silver nanoparticles directly onto TEM support films. Silver nanoparticles were obtained from nanoComposix and used without further purification. Our experiments utilized two types of TEM grids: (1) a copper grid coated with 2–3 nm of amorphous carbon on Formvar (Ted Pella, Inc. #01822) and (2) 20 nm supported SiN_x membrane (SPI Supplies #4105SN). Prior to use the carbon grid was cleaned with HPLC grade chloroform to remove the Formvar. These grids were chosen to allow comparison of STEM/EELS measurements on both

conducting and nonconducting substrates. The SiN_x support produced superior results, due to a more even dispersion of the nanoparticles on this surface, and a higher signal-to-noise ratio in the optical scattering measurements. A 2 μL aliquot of the colloidal sample was drop-coated directly onto the TEM support, and the solvent was allowed to evaporate. Once the silver nanoparticles had been deposited, the sample was placed on a coverslip, mounted in a custom designed sample holder, and purged with dry nitrogen in order to remove water on the nanoparticles and grid.

First, resonance-Rayleigh scattering measurements were performed on a series of individual particles, and wide-field images were collected to serve as maps to enable the location of the same nanoparticles during subsequent STEM measurements. Scattering measurements were performed using an inverted microscope (Nikon, Ti-U) equipped with a dark field condenser (Nikon, NA = 0.95–0.80). The excitation source was the unpolarized output of a tungsten–halogen lamp. Scattered light from an individual nanoparticle was collected with a 100 \times (Nikon, 0.7 < NA < 1.4, oil immersion) objective and coupled into a dispersive imaging spectrometer (Acton Research, $f = 0.3$ m) using a $f = 5.0$ cm lens. Light was detected on a liquid nitrogen cooled back-illuminated

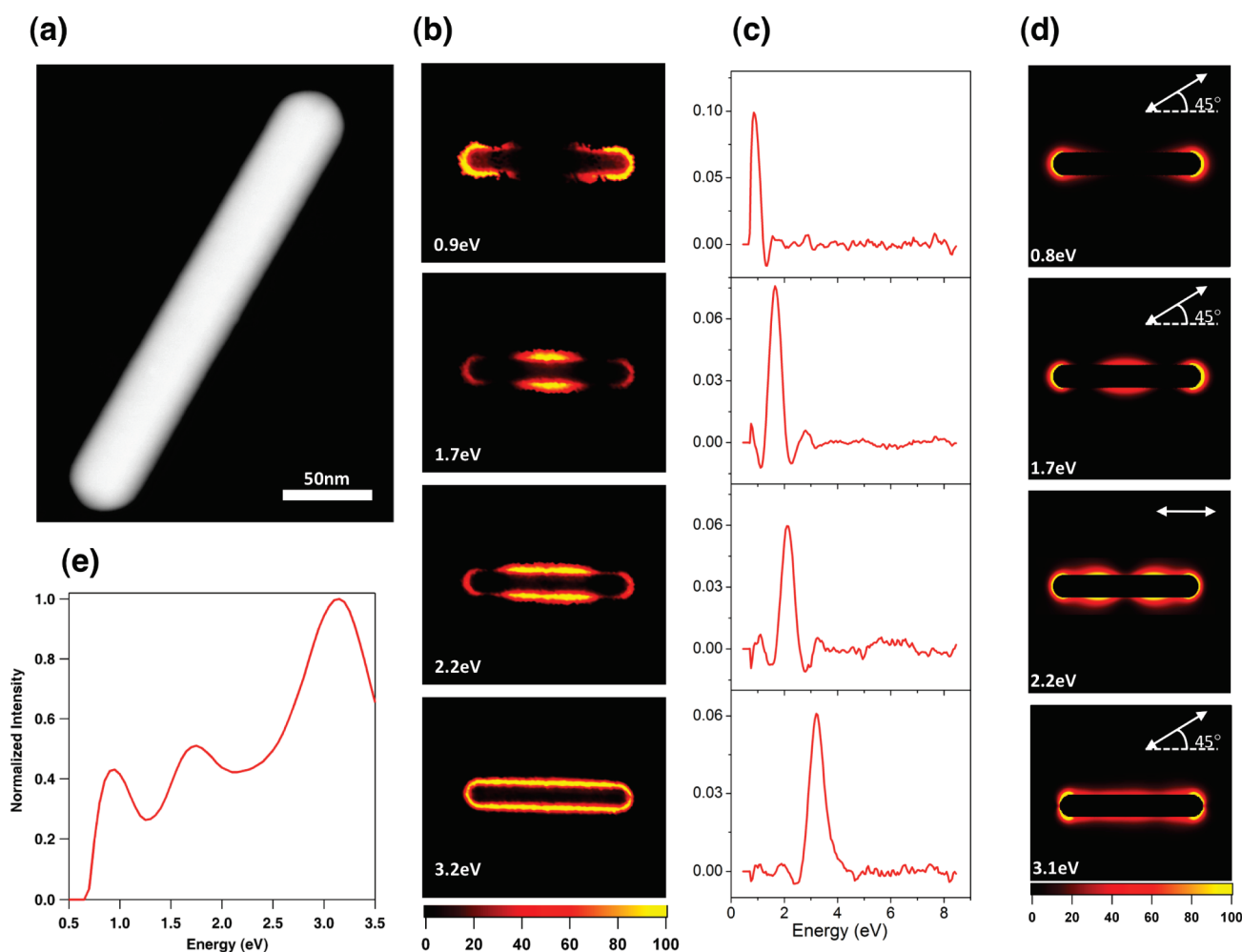


Figure 2. EELS data and electrodynamic calculations for rod 2. (a) ADF image of the rod: length = 267 nm, diameter = 42 nm, aspect ratio = 6.4. (b) MVSA score images, and (c) loading spectra, for each component, interpreted as plasmon maps and energies, respectively. From a total of 11 components found by MVSA, two components were considered overlapping and combined to form the $E = 0.9$ eV mode, two were combined to form the $E = 3.2$ eV mode, and two are displayed as found. (d) DDA calculated electric field plots displaying the field generated by a plane wave optical excitation at the energies and polarizations given on each panel. (e) Summed EEL spectrum.

charge couple detector (CCD) (Princeton Instruments, PIXIS 100). The dark-field scattering spectrum of each individual nanoparticle was obtained using a 150 grooves/mm grating with a 500 nm blaze. Similar to a procedure described by Wang et al.,²⁵ a wide-field image of the silver nanoparticles on the TEM grid was also recorded to serve as a map for subsequent location in the STEM. This method enabled correlated optical and STEM measurements from the same nanostructures.

After particles of interest had been identified from the optical characterization, the sample was inserted into a dedicated aberration-corrected, cold-field-emission STEM. Using the optical maps, each nanoparticle was found in turn and an EEL spectrum imaging (SI) map collected from the zero-loss-peak containing region. In each case the rod in question was found by comparison of the optical map to the pattern of particles imaged in the STEM at very low resolution; after identification, a higher resolution annular dark field (ADF) image was collected (Figures 1a, 2a, and 3a), followed by the SI. The STEM EELS spectrum imaging measurement was performed on a VG Microscopes HB501UX STEM with Nion aberration corrector and Gatan Enfina EEL spectrometer. The spectrometer dispersion

was set to 0.05 eV per channel with an exposure time of 0.05 s per spectrum. The pixel size/density was chosen to give a total acquisition time of around 15 min for a single SI. The energy resolution (as measured by the fwhm of the zero loss peak) was ~ 0.45 – 0.50 eV. The data presented in this paper come from particles identified unambiguously as the same particles from which optical data were collected.

Next, we simulated the optical response and local field enhancements using the discrete dipole approximation (DDA),^{26,27,17,28} by the DDSCAT7.0 program.²⁹ In the DDA, silver rods are represented as a cubic array of polarizable elements whose polarizability is determined from the nanoparticle dielectric function.^{26,30} The silver rods discussed in this report were modeled as cylinders with a hemispherical cap at each end. Dipoles are induced as a result of the interaction of the polarizable elements with an incident plane wave field and with fields arising from the other polarizable elements. The fields outside the nanoparticle are determined from the superposition of the incident plane wave and the fields of the induced dipoles. These fields are calculated half a grid spacing from the surface, instead of right on the surface, in order to avoid numerical instabilities that

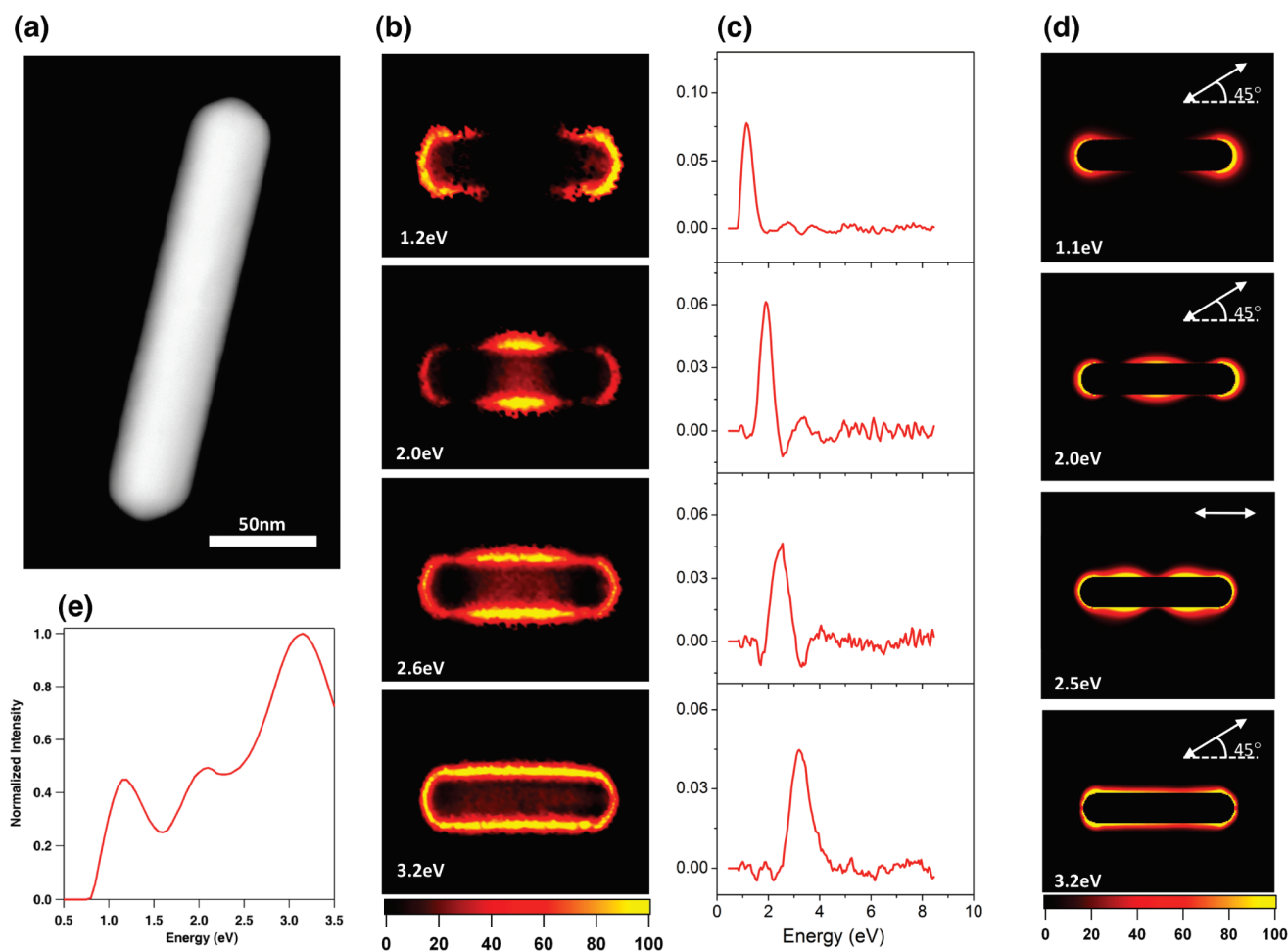


Figure 3. EELS data and electrodynamic calculations for rod 3. (a) ADF image of the rod: length = 202 nm, diameter = 40 nm, aspect ratio = 5.1. (b) MVSA score images, and (c) loading spectra, for each component, interpreted as plasmon maps and energies, respectively. From a total of 12 components found by MVSA, two components were considered overlapping and combined to form the $E = 1.2$ eV mode, two were combined to form the $E = 3.2$ eV mode, and two are displayed as found. (d) DDA calculated electric field plots displaying the field generated by a plane wave optical excitation at the energies and polarizations given on each panel. (e) Summed EEL spectrum.

arise at the surface. The grid spacing used was 1 nm and the dielectric constants of silver were from Palik.³¹ The refractive index of the surrounding medium was fixed at a value of 1.35 to include the substrate effect implicitly. It is known that the optical scattering spectra of nanoparticles can depend on the solid angle of collection; this effect is not modeled in our electrodynamic simulations. In our current measurements the use of a high numerical aperture objective should minimize these effects, although studies exploring the dependence of the scattering spectra on the polarization and solid angle of collection are an interesting avenue of future research.

Data analysis for high-aspect-ratio particles is especially challenging due to the large number of overlapping (both spatially and spectrally) LSP modes.²⁴ To extract the experimentally measured modes from our data, we employed MVSA, using the Automated eXpert Spectral Image Analysis (AXSIA) program developed by Keenan and co-workers.^{32–34} This software uses a combination of principal components analysis (PCA) with matrix rotation to maximize spectral contrast,³⁴ thus improving the interpretability of the individual components.³⁵ The resulting decomposed data comprised spatial maps of the individual LSP component spectra, which we were able to compare with the simulated field plots.

To perform the data analysis, first the zero loss peak (ZLP) was fit to a Gaussian plus Lorentzian using Gatan Digital Micrograph software; peak centering at zero electron volts was performed to align the individual spectra, and a ZLP subtraction was performed. Examination of the spectrum image before deconvolution reveals a progression of overlapping modes—energy slices of these data for rod 1 are given in Figure S1 (Supporting Information). Noise reduction is achieved using MVSA methods, which extract the experimentally measured modes using a PCA followed by matrix rotations, using AXSIA.^{32,34} MVSA methods decompose SI data into spatial- and spectral-component matrices. The procedure applied by AXSIA first scales the data for non-Gaussian noise.^{36,37} This so-called optimal-scaling normalization or Poisson-scaling method was used to account for the nature of the noise in the data,³⁶ whereby higher signal levels are contaminated by noise in proportion to the signal and therefore need to be down-weighted prior to MVSA (lest such algorithms fit noise at the expense of weaker but relevant spectral information). An eigenanalysis was then performed on the scaled data in order to determine the pseudo- or chemical-rank of the decomposed spectral and spatial matrices. Normally, the sorted eigenvalues are interrogated

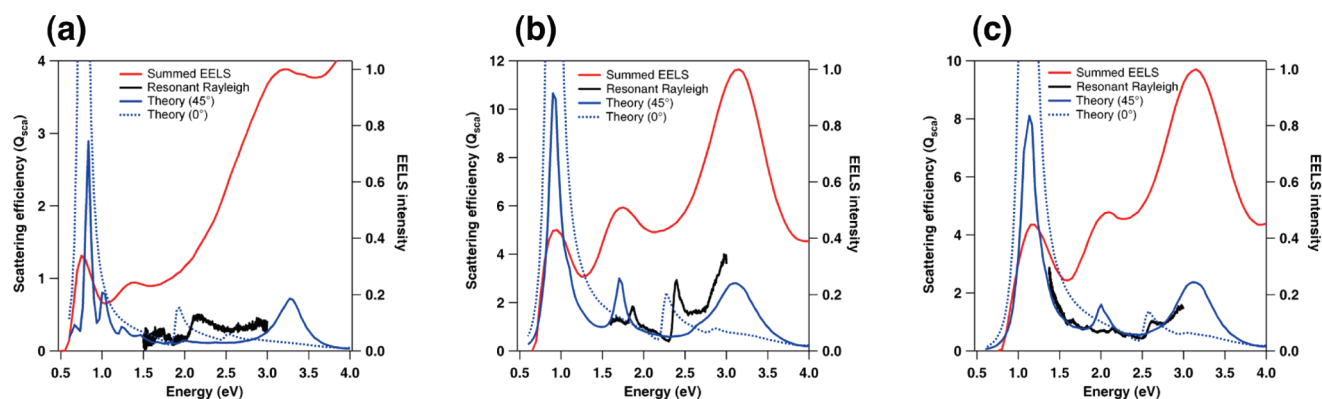


Figure 4. Comparison of spectra collected/simulated for each rod: (a) rod 1; (b) rod 2; (c) rod 3. The EEL spectrum in each case (shown in red) is the sum of all spectra from the SI after zero-loss-peak centering and removal: black, experimental resonant-Rayleigh scattering spectra; blue, theoretical calculations of the scattering spectra for polarizations at 0° and 45° with respect to the rod axis (dotted and solid lines, respectively). The experimental spectra for rod 1 (a) was obtained on a C support film whereas rods 2 and 3 ((b) and (c)) were supported on a SiN_x membrane.

manually but AXSIA employs an automated routine to discriminate noise from non-noise components (the so-called breakpoint in the aforementioned plot). In principle, this reduced rank approximation of the data provides a succinct description of the signal and suppresses the experimental noise. PCA is then performed on the scaled data with the previously determined pseudorank prescribing the number of retained components. The AXSIA software allows additional manipulation of the data in the form of matrix rotations, which in the case of the data presented here maximizes the spectral components' mutual simplicity (or contrast) and is used to improve the interpretability of the individual components. The resulting decomposed data comprised two matrices which include spatial components and respective spectral components, each displaying one well-defined peak, which we took to represent the plasmon mode and its corresponding spectrum or energy. Before AXSIA was run, the centered and ZLP-subtracted data were truncated to the region of interest (a wide energy range of 0.45–8.45 eV was chosen, to avoid deleting relevant information), and the noise normalization,^{36,37} PCA decomposition, rotation of the spectral components via the Varimax procedure³⁴ and related inverse rotation of the spatial components, and inverse noise normalization to return to real counts from scaled counts were performed. Specifically, the operations performed by AXSIA are, in the following order: (1) a Poisson scaling;^{36,37} (2) a PCA, resulting in orthogonal spatial components and orthonormal spectral components; (3) a rotation of the orthonormal spectral basis using Varimax³⁴ and an inverse rotation of the spatial components which as a result are no longer orthogonal; (4) an inverse Poisson scaling to return to physical count space from Poisson space, resulting in spectral and spatial components which are now both oblique. These resultant matrices nonetheless retain the relevant and interpretable spectral and spatial information. It should be noted for clarity that while the title of Keenan et al.³⁴ is concerned with “spatial-domain simplicity”, the paper is more general and discusses the method underlying “spectral-domain simplicity” as applied here.

Figures 1–3 compare experimental and theoretical plasmon maps for three nanorods analyzed in this way. In the case of all three rods four or more components are resolved in the 0.5–4.0 eV region (Figures 1–3, panels b and c). Where individual rotated PCA components appeared to display the same symmetry and were separated in energy by less than the spectral

resolution of the measurement (~ 0.45 eV) we superimposed them into a single component; this is noted in the figure caption where it applies, and all of the uncombined modes are displayed in the Supporting Information (Figures S2–S4). Figures 1–3 represent the first demonstration of an experimental mapping of plasmon modes at this level of complexity. In each case dipolar modes are observed below 1 eV, followed by a series of quadrupolar and higher multipolar modes with increasing numbers of nodes for increasing energy, with transverse modes emerging above 3 eV. Our approach is shown to be general by the consistency of the results between the different rods. As expected, additional multipolar modes emerge as the rod aspect ratio increases (e.g., Figure 1 versus Figures 2 and 3), and the mode energy increases with decreasing aspect ratio. The EEL spectra displayed in each figure (Figures 1e, 2e, and 3e) are the sum of all the spectra from the centered, ZLP-removed SI, before MVSA.

The calculated field-enhancement plots obtained from plane wave excitation, given as $|E_{\text{loc}}|^2/|E_0|^2$, are in excellent agreement with both the energy and spatial distribution of the MVSA extracted plasmon maps. This agreement is quite striking given the simplicity of our theoretical approach and suggests a more general applicability of EELS to the mapping of optically driven plasmons. In some cases the nodes in the experimentally determined plasmon maps are not as clearly demarcated as in the theoretical plots and we attribute this to the finite energy resolution of the experiment (e.g., the $E = 2.2$ eV mode in panels b and d of Figure 2). In the electrodynamics calculations, excitation of all experimentally observed plasmon modes is not possible with the polarization parallel to the rod axis; the inactive modes, however, are active when the laser polarization is rotated 45° with respect to the rod axis. The slight asymmetry of the field plots in these cases, resulting from retardation effects,³⁸ has been reduced by taking an average of the $+45^\circ$ and -45° polarization directions. The polarization direction in each case is indicated in the figure inset.

Figure 4 presents a comparison of the summed EELS spectra with the experimentally measured resonance-Rayleigh spectra and the theoretically calculated nanorod scattering spectra. In each case, the total EEL spectrum exhibits three broad peaks which we attribute to collections of plasmon components in order of increasing energy: dipolar, multipolar, and transverse. The peak positions of the longitudinal (dipole <1 eV) and

transverse (>3 eV) modes in the theoretically calculated optical scattering spectra correlate well with peaks in the EEL spectra. There are differences in intensity as might be expected since the excitation mechanism in each case is different, i.e., plane wave versus electron beam. Figure 4 also compares the experimental resonance-Rayleigh spectra with simulated scattering spectra. The modes with the strongest optical activity are the dipolar modes (<1 eV) and the bulk plasmon modes (>3 eV); however, the optical data are limited to the visible region of the spectrum (1.5–3.0 eV) and does not encompass these modes. In the measured energy range the scattering features, e.g., the 1.8 and 2.4 eV experimental modes in Figure 4b, are estimated to be an order of magnitude smaller than the dipolar scattering peak. Despite this fact, we still find that the main features in the experimental scattering spectra are reproduced in the theoretical scattering spectra. The small shifts between the theoretical and experimental peak positions result because these weak modes are particularly sensitive to the dielectric environment. While the agreement between our electrodynamics simulations and the experimental scattering spectra is not quantitative, the agreement between the calculated electric field enhancement plots and EELS maps is striking (Figures 1–3). These data taken together suggest that correlated studies such as these will ultimately provide a unified picture of optical and electron beam excited plasmons. Further, it reinforces the notion that plasmon maps derived from EELS excitation have direct relevance for the plethora of processes relying on optical excitation of plasmons.

A comparison of optical scattering measurements or individual EEL spectra (Figure 4), with that obtained from a MVSA of the EEL SI (Figures 1–3) reveals that vastly more information is available by utilizing EELS mapping. Where the optical spectrum measures only specific allowed transitions within a limited energy range, and the summed EEL spectrum shows overlapping collections of modes, MVSA reveals all of the symmetries and energies predicted by simulation—including both bright and dark modes, with spatial resolution on the length scale of the plasmon itself. It is clear from comparison of the summed EEL spectra with the MVSA deconvoluted EELS plasmon maps that the relatively low energy resolution of the electron microscope leads to such great spectral overlap of modes that they cannot be identified without spatial mapping combined with deconvolution. For complex or high aspect ratio nanostructures, it is insufficient to take individual spectra, even from a series of points on an image, nor will energy slices (such as produced by EFTEM imaging) properly separate modes with close spectral overlap. We also believe that correlated optical and EELS measurements from the exact same nanostructure are necessary to understand the connection between photon and electron excited plasmons. Low-energy-loss EEL SI mapping with MVSA analysis, when combined with correlated optical scattering data and electrodynamics modeling, therefore provides an invaluable method for the characterization of plasmonic nanostructures whose complexity will only continue to increase in the future.

■ ASSOCIATED CONTENT

S Supporting Information. Additional figures showing energy slices of the spectrum image from rod 1 before MVSA (Figure S1) and all of the uncombined components for all three rods found by MVSA (Figures S2, S3, and S4). This material is available free of charge via the Internet at <http://pubs.acs.org>.

■ AUTHOR INFORMATION

Corresponding Author

*E-mail: beth.guilton@uky.edu (B.S.G.) or jcamden@utk.edu (J.P.C.).

■ ACKNOWLEDGMENT

This research was supported by the Eugene P. Wigner Fellowship program of Oak Ridge National Laboratory (B.S.G.); UT Knoxville start up grant, the UT/ORNL Joint Institute for Advanced Materials, and the U.S. Department of Energy, Office of Basic Energy Sciences under Award Number DE-SC0004792 (J.P.C.); Start up grant of NTU and AcRF Tier 1 grant (RG 43/10) of Singapore MoE (S.L.); Oak Ridge National Laboratory's SHaRE User Facility (C.M.P.), which is sponsored by the Office of Basic Energy Sciences, U.S. Department of Energy; Sandia (P. G.K.) is a multiprogram laboratory operated by Sandia Corporation, a Lockheed Martin Company, for the United States Department of Energy's (DOE) National Nuclear Security Administration (NNSA) under Contract DE-AC0494AL85000; DOE BES Grant DE-SC0004752 (G.C.S., S.L.); and the Office of Basic Energy Sciences, Materials Sciences and Engineering Division, U.S. Department of Energy (S.J.P., M.V., D.N.L.). Roles and responsibilities: B.S.G., S.J.P., and J.P.C. designed the experiments; B.S.G., V.L., D.N.L., and M.V. collected and analyzed the data; C.M.P., P.G.K., and B.S.G. performed the MVSA; S.L. and G.C.S. performed the theoretical calculations; all authors participated in the discussion and analysis of the results and read and commented on the final manuscript.

■ REFERENCES

- (1) Maier, S. A. *Plasmonics: Fundamentals and Applications*, 1st ed.; Springer-Verlag: New York, 2007.
- (2) Kelly, K. L.; Coronado, E.; Zhao, L. L.; Schatz, G. C. *J. Phys. Chem. B* **2003**, *107*, 668–677.
- (3) Maier, S. A. *IEEE J. Sel. Top. Quantum Electron.* **2006**, *12*, 1671–1677.
- (4) Maier, S. A.; Kik, P. G.; Atwater, H. A.; Meltzer, S.; Harel, E.; Koel, B. E.; Requicha, A. A. G. *Nat. Mater.* **2003**, *2*, 229–232.
- (5) Sannomiya, T.; Hafner, C.; Voros, J. *Nano Lett.* **2008**, *8*, 3450–3455.
- (6) Nie, S.; Emory, S. R. *Science* **1997**, *275*, 1102–1106.
- (7) Kneipp, K.; Wang, Y.; Kneipp, H.; Perelman, L. T.; Itzkan, I.; Dasari, R. R.; Feld, M. S. *Phys. Rev. Lett.* **1997**, *78*, 1667.
- (8) Haran, G. *Acc. Chem. Res.* **2010**, *43*, 1135–1143.
- (9) Batson, P. E. *Phys. Rev. Lett.* **1982**, *49*, 936.
- (10) Bosman, M.; Keast, V. J.; Watanabe, M.; Maarouf, A. I.; Cortie, M. B. *Nanotechnology* **2007**, *18*, 165505.
- (11) Nelayah, J.; Kociak, M.; Stéphan, O.; García de Abajo, F. J.; Tencé, M.; Henrard, L.; Taverna, D.; Pastoriza-Santos, I.; Liz-Marzán, L. M.; Colliex, C. *Nat. Phys.* **2007**, *3*, 348–353.
- (12) Keast, V. J.; Bosman, M. *Mater. Sci. Technol.* **2008**, *24*, 651–659.
- (13) Arslan, I.; Hyun, J. K.; Erni, R.; Fairchild, M. N.; Hersee, S. D.; Muller, D. A. *Nano Lett.* **2009**, *9*, 4073–4077.
- (14) Chu, M.-W.; Myroshnychenko, V.; Chen, C. H.; Deng, J.-P.; Mou, C.-Y.; García de Abajo, F. J. *Nano Lett.* **2009**, *9*, 399–404.
- (15) Gu, L.; Sigle, W.; Koch, C. T.; Nelayah, J.; Srot, V.; van Aken, P. A. *Ultramicroscopy* **2009**, *109*, 1164–1170.
- (16) Nelayah, J.; Gu, L.; Sigle, W.; Koch, C. T.; Pastoriza-Santos, I.; Liz-Marzán, L. M.; van Aken, P. A. *Opt. Lett.* **2009**, *34*, 1003–1005.
- (17) N'Gom, M.; Li, S.; Schatz, G.; Erni, R.; Agarwal, A.; Kotov, N.; Norris, T. *Phys. Rev. B* **2009**, *80*, 113411.
- (18) Schaffer, B.; Hohenester, U.; Trügler, A.; Hofer, F. *Phys. Rev. B* **2009**, *79*, 041401.
- (19) Sigle, W.; Nelayah, J.; Koch, C. T.; van Aken, P. A. *Opt. Lett.* **2009**, *34*, 2150–2152.

- (20) de Abajo, F. *Rev. Mod. Phys.* **2010**, *82*, 209–275.
- (21) Schaffer, B.; Grogger, W.; Kothleitner, G.; Hofer, F. *Ultramicroscopy* **2010**, *110*, 1087–1093.
- (22) Koh, A. L.; Fernández-Domínguez, A. I.; McComb, D. W.; Maier, S. A.; Yang, J. K. W. *Nano Lett.* **2011**, *11*, 1323–1330.
- (23) Hohenester, U.; Ditlbacher, H.; Krenn, J. R. *Phys. Rev. Lett.* **2009**, *103*, 106801.
- (24) Koh, A.; Bao, K.; Khan, I.; Smith, W.; Kothleitner, G.; Nordlander, P.; Maier, S.; McComb, D. *ACS Nano* **2009**, *3*, 3015–3022.
- (25) Wang, Y.; Eswaramoorthy, S. K.; Sherry, L. J.; Dieringer, J. A.; Camden, J. P.; Schatz, G. C.; Van Duyne, R. P.; Marks, L. D. *Ultramicroscopy* **2009**, *109*, 1110–1113.
- (26) Draine, B. T.; Flatau, P. J. *J. Opt. Soc. Am. A* **2008**, *25*, 2693–2703.
- (27) Li, S.; Pedano, M. L.; Chang, S. H.; Mirkin, C. A.; Schatz, G. C. *Nano Lett.* **2010**, *10*, 1722–1727.
- (28) Zhang, J.; Li, S.; Wu, J.; Schatz, G. C.; Mirkin, C. A. *Angew. Chem., Int. Ed.* **2009**, *48*, 7787–7791.
- (29) Draine, B. T.; Flatau, P. J. Arxiv preprint arXiv:0809.0337, 2008.
- (30) Draine, B. T.; Flatau, P. J. *J. Opt. Soc. Am. A* **1994**, *11*, 1491.
- (31) Lynch, D. W.; Hunter, W. R. *Handbook of Optical Constants of Solids*; Academic Press: New York, 1985.
- (32) Kotula, P. G.; Keenan, M. R.; Michael, J. R. *Microsc. Microanal.* **2003**, *9*, 1–17.
- (33) Ohlhausen, J. A.; Keenan, M. R.; Kotula, P. G.; Peebles, D. E. *Appl. Surf. Sci.* **2004**, *231*, 230–234.
- (34) Keenan, M. *Surf. Interface Anal.* **2009**, *41*, 79–87.
- (35) Smentkowski, V.; Ostrowski, S.; Keenan, M. *Surf. Interface Anal.* **2009**, *41*, 88–96.
- (36) Keenan, M.; Kotula, P. *Surf. Interface Anal.* **2004**, *36*, 203–212.
- (37) Keenan, M.; Kotula, P. *Appl. Surf. Sci.* **2004**, *231*, 240–244.
- (38) Payne, E. K.; Shuford, K. L.; Park, S.; Schatz, G. C.; Mirkin, C. A. *J. Phys. Chem. B* **2006**, *110*, 2150–2154.